Available online at www.sciencedirect.com

ScienceDirect

Ceramics International 39 (2013) 9683–9690

CERAMICS INTERNATIONAL

www.elsevier.com/locate/ceramint

Numerical simulation of cold isostatic pressed alumina parts produced by selective laser sintering and part shape optimization

Wenting He, Qingsong Wei, Kai Liu, Yusheng Shi*, Jie Liu

Material Forming and Mould State Key Laboratory, School of Material Science and Engineering, Huazhong University of Science and Technology, Wuhan 430074, China

Received 5 March 2013; received in revised form 13 April 2013; accepted 24 April 2013
Available online 14 May 2013

Abstract

Cold isostatic pressing (CIP) combined with selective laser sintering (SLS) is a practical and effective process for producing complex ceramic components with high density. This paper focused on the numerical simulation of alumina SLSed components during CIP for near net shaping. The Drucker–Prager-Cap plasticity model was used to predict the densification behavior and deformation of the alumina/epoxy resin composite powders. CIP experiments were conducted to determine the required parameters for the model. The simulative final dimensions and densities agree well with the experimental results, with the relative error less than 1.7% in the forming plane. Structure optimization was made to the part and bag, which proves conducive to reducing distortion. The effects of the part fillet radius on shape accuracy were investigated, and the optimal fillet radius can be determined by simulation. Eventually, the alumina part reached its highest density of 94.5% through optimized CIP and sintering process.

Keywords: Alumina; Cold isostatic pressing; Numerical simulation; Selective laser sintering

1. Introduction

Structural ceramics such as alumina are characterized with high hardness and brittleness, giving rise to the difficulties in processing ceramic components by the conventional forming methods [1]. Although slip casting and gelcasting can shape high-density components with complex structures, the costs and the difficulties of producing molds and discharging organics are increased [2]. Selective laser sintering (SLS) is an additive manufacturing technique which can shape complex parts without any molds or preformed blanks [3]. It can meet the demand of manufacturing complicated ceramic parts. But one of the biggest disadvantages of SLS is the low density of the formed porous parts.

Cold isostatic pressing (CIP) can densify powders or porous parts as well as homogenize density distribution [4]. The SLS/CIP compound process can overcome the difficulties of CIP in manufacturing complex bags. Therefore, it is a promising way to combine SLS and CIP to shape complex ceramic components. Recently, Shahzad et al. have prepared alumina/PA composite powders to manufacture SLSed components which were densified by CIP and high temperature sintering later. The final density of the resulted alumina components reached 88%, which needs to be further increased. And their work did not involve the prediction of final shape and part density after CIP. These two aspects are however of great significance to the precision control of the compound process [5].

For current CIP process, trial and error methods are adopted to design the initial shape of bags and components, which turn out to be time-consuming and less accurate. Finite element simulation (FEM) is an effective tool to assist in predicting part deformation and understanding the densification behavior as well as the effects of bags on the process. Although many scholars have successfully applied FEM methods to illustrate the CIP process of ceramic, metal powders and even metallic SLSed parts [6–9], the numerical simulation of alumina SLSed parts during CIP has not been reported in literature. Despite that the material and component type analyzed in this paper is different from the previous study, a 3D model is developed considering the multiple interaction between bag and part in

*Corresponding author. Tel.: +86 138 7134 4486; fax: +86 027 8755 8155.
E-mail address: hewenting1127@qq.com (Y. Shi).

0272-8842/$ - see front matter © 2013 Elsevier Ltd and Techna Group S.r.l. All rights reserved.
http://dx.doi.org/10.1016/j.ceramint.2013.04.086

3D space. Moreover, structure optimization of parts or bags by the use of simulation were less reported.

In this work, the Drucker–Prager-Cap constitutive model is utilized to predict the densification and deformation of alumina SLSed components during CIP. Based on the comparison between the simulative and experimental results, proper structure optimization for the component and bag is supposed to enhance the process accuracy.

2. Constitutive models

It is well known that continuum plastic models are always used to describe the densification behavior and mechanical response of powder materials during compaction process. Due to the porous structures of SLSed components, their mechanical properties are similar to that of the cohesive geological materials. Our work is based on the Drucker–Prager-Cap model [10], the typical clay plasticity constitutive model to describe the process. The yield surface of the model consists of two segments, a pressure-dependent Drucker–Prager shear failure segment and a compression cap yield segment, which is shown in Fig. 1. The Drucker–Prager shear failure surface can be written as [10]:

$$F_s = q - p\tan\beta - d = 0 \tag{1}$$

where β and d denote the friction angle and cohesion of the material respectively; q is Mises equivalent stress, defined as $q = \sqrt{3S : S/2}$, where S denotes the deviatoric stress, p is isostatic pressure.

On the Cap surface, plastic flow leads to compaction. The Cap yield surface is:

$$F_c = \sqrt{(p - p_a)^2 + (Rq/(1 + \alpha - \alpha/\cos\beta))^2} - R(d + p_a\tan\beta) = 0 \tag{2}$$

Where R is a material parameter that controls the shape of the cap, p_a is an evolution parameter that represents the volumetric inelastic strain driven hardening, α is a small variable used to define a transition yield surface (ranging from 0.01–0.05).

A Neo-Hookean hyperelastic model is utilized to describe the instantaneous hyperelastic response of the rubber bags, which are assumed as incompressible isotropic elastomers. The Neo-Hookean strain energy potential is written as:

$$U = C_{10}(\overline{I}_1 - 3) + (J^{el} - 1)/D_1 \tag{3}$$

where U is the strain energy per unit of reference volume; C_{10} and D_1 are temperature-dependent material parameters, which are considered constant in this work; J^{el} is the elastic volume ratio and $\overline{I}_1$ is the first deviatoric strain invariant defined as $\overline{I}_1 = \overline{\lambda}_1^2 + \overline{\lambda}_2^2 + \overline{\lambda}_3^2$. Where the deviatoric stretched $\overline{\lambda}_1 = J^{-1/3}\lambda_i$, λ_i are the principal stretches.

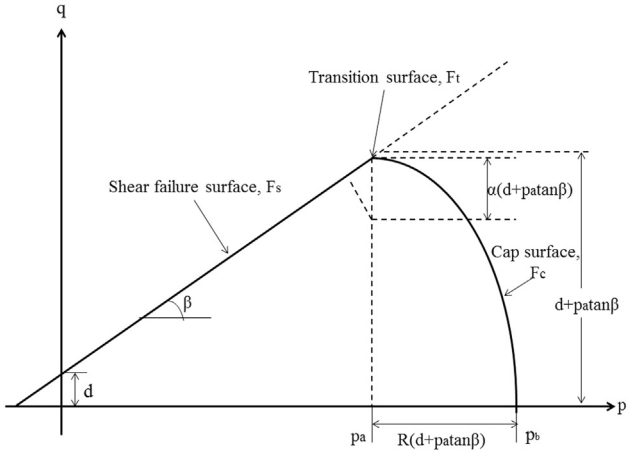

Fig. 1. The yield surface of the Drucker–Prager-Cap model in p–q plane.

3. Material and method

3.1. Materials and experiments

In this present paper, a composite powder (Fig. 2(a)) was made by ball milling of the mixture of the matrix material and the binder, namely granulated alumina powder with an average particle size of 80 μm (Fig. 2(b)) and epoxy resin E06 powder (d_{50}∼50 μm, Xinyinhe, China) respectively. The granulated alumina was prepared by spraying 1.5 wt% Polyvinyl Alcohol (PVA) to the initial α-Al_2O_3 powder (grade SM8, d_{50}∼0.8 μm, Chinalco, China). The granulated alumina powder accounts for 92% of the composite powder in weight. The chemical composition of the granulated alumina powder is shown in Table 1. First of all, several cuboid components were made with the powder by HRP-IIA type SLS rapid prototyping system (Huazhong University of Science and Technology) for repeated measurement. The optimal processing parameters obtained from the density orthogonal experiments are listed in Table 2. Then the components were dipped into the natural rubber latex at 85 °C for 2 h, which would make coatings with a thickness of approximately 1 mm around the components. Eventually, the components were pressed in a CIP apparatus under 320 MPa.

Additionally, a set of test specimens were CIPed to get the hardening properties of the composite powder. The volumetric plastic strains of the specimens were measured respectively under the hydrostatic pressure of 50, 100, 150, 200, 260, 300 and 320 MPa. The fitted curve of hydrostatic pressure versus volumetric plastic strain was plotted in Fig. 3, where the volumetric plastic strain ε_{vol}^p is given as $\varepsilon_{vol}^p = \varepsilon_{11} + \varepsilon_{22} + \varepsilon_{33}$. ε_{11}, ε_{22}, and ε_{33} are the principal plastic strain in three perpendicular directions, p denotes hydrostatic pressure. The function of fitted curve is:

$$p = 7.03\exp(6.46\varepsilon_{vol}^p) \tag{4}$$

Then the CIPed parts were degreased under the determined degreasing process according to the thermal gravity analysis (TGA) curve of the composite powder. During the resin burn-out and sintering process, the polymer contents were decomposed and discharged by degreasing furnace, thus relatively pure porous parts were obtained. The alumina part density was further improved by and the following high temperature solid sintering. The optimized parameters of high temperature sintering are set as: sintering temperature 1600 °C, holding time 4 h and temperature increasing rate 2 °C/h.

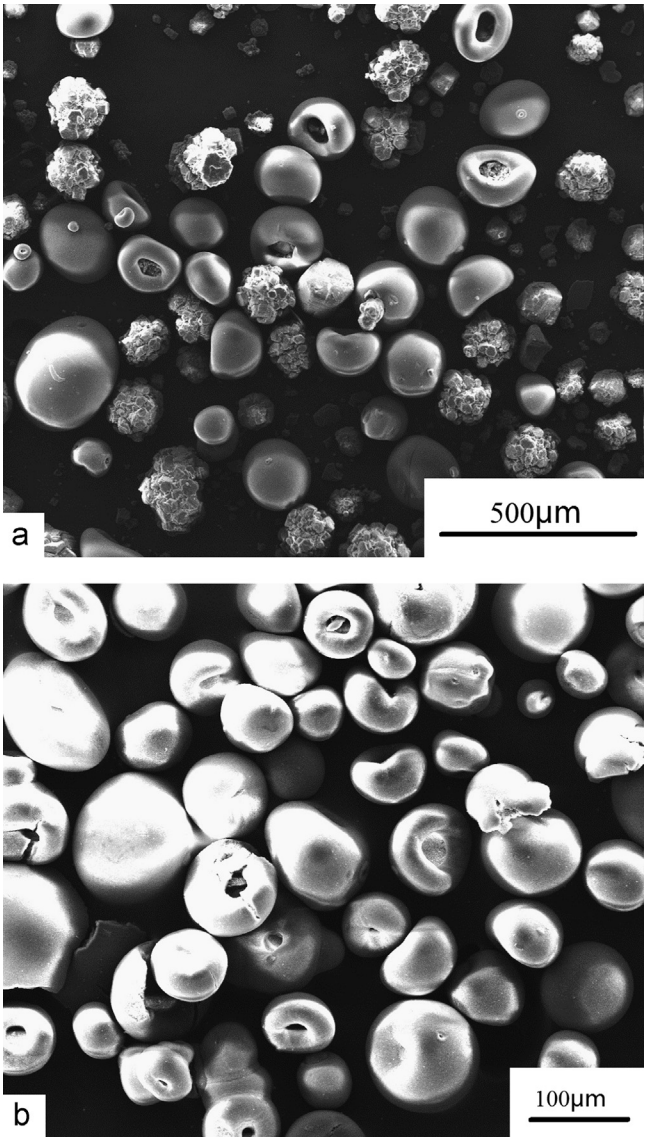

Fig. 2. The SEM micrographs of powders: (a) the composite powder, and (b) granulated alumina powder.

Table 1
Composition of α-Al_2O_3 granulated powder (ω/%).

Al_2O_3	Fe_2O_3	Na_2O	PVA
≥98	≤0.03	≤0.05	≤1.5

3.2. Finite element simulations

Commercial FE software Abaqus/Explicit was utilized to analyze the densification behavior and deformation of the alumina cuboid component during CIP. The dimensions of the component are listed as 51.20 mm in length, 11.00 mm in width and 9.80 mm in height. In order to fully investigate the multiple interactions in 3D space during CIP, the one eighth of the cuboid component was taken as the analysis model according to its symmetry. The influence of rubber bags was involved with a thickness of 1 mm by the Neo-Hookean model. A hydrostatic pressure of 320 MPa was applied on the surfaces of the bag model. Besides, 8-node linear brick elements with reduced integration were applied to both the part and the bag. As shown in Fig. 4, to solve the converging problems for contacting surfaces, suitably refined meshes were scattering in different regions of the bag model. The Z axis is vertical to the laser scanning plane. Other required parameters such as d, R, and β are referred to those in Canto et al. [11]. Sliding friction coefficient μ was assumed as 0.2.

Table 2
The optimized parameters for SLS through orthogonal experiments.

Laser power (W)	Scanning speed (mm/s)	Scanning space (mm)	Thickness of powder layer(mm)
15	1600	0.1	0.15

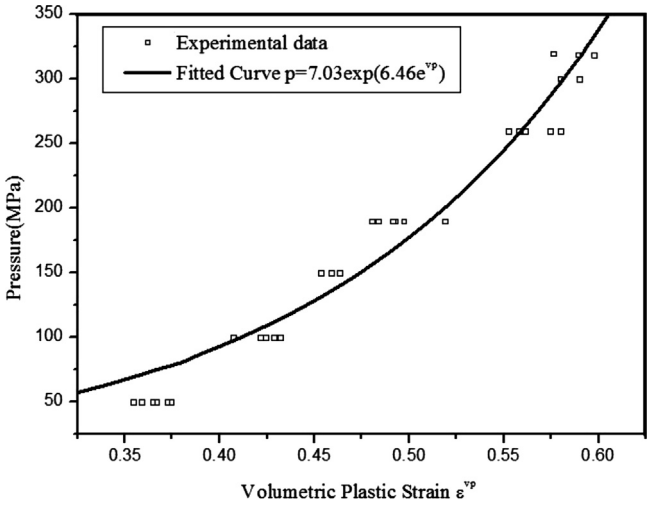

Fig. 3. Curve of volumetric plastic strain versus hydrostatic pressure of the composite powder.

4. Results and discussion

4.1. CIP simulation and experimental verification of cuboid components under the influence of bags

As shown in Table 3, the simulative dimensions agree well with the experimental results, with the relative error less than 1.7% in the forming plane. It is notable that the experimental shrinkage rate along the layer thickness is much larger than that in laser forming plane. It is mainly due to the structure anisotropy of SLSed components, resulted from the laser scanning strategy [12].

Obvious protuberance along edges is found in Fig. 4. Theoretically, it has been proved that the ratio of the stiffness of the part and that of bag controls the distortion during the compaction process [13]. While in the initial stage of CIP, the porous structure of the SLSed part makes it much softer than its theoretical stiffness. The part shape changes with the serious deformation of the bag. Thus the edges and corners are distorted and become sharper. Fig. 5(a) and (b) shows the shear strain and relative density distribution of the part

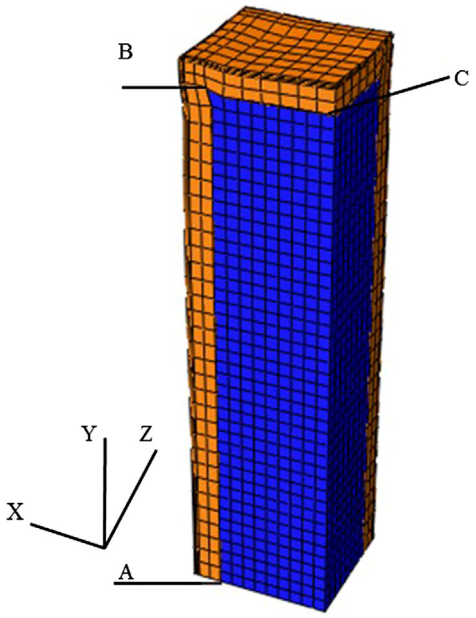

Fig. 4. The deformation and mesh of cuboid model after CIP.

respectively. Since the corners and edges become sharper, shear stress grows sharply in these areas, which in turn makes the distortion more serious. Consequently, the compression strain decreases in these areas, resulting in their low density. Fig. 6 shows the comparison between experimental and predicted final shape. The geometrical shape was measured by a 3D measurement device (Huazhong University of Science and Technology). Both geometries reach excellent agreement, with the maximum dimensional error less than 0.2 mm. Besides, the significant influence of bags on part distortion and final shape is addressed in simulation. According to Figs. 7 and 8, the maximum displacement difference of AB path (namely the displacement difference between node A and B, shown in Fig. 7) along X direction is $-0.808-(-1.036)=0.228$(mm), and the maximum difference of the displacement of BC path along Y direction is 0.193 mm. The distortion of the two paths is obvious due to the large shear stress. It implies bag still has negative effects on shape accuracy during compaction.

Fig. 9 shows the evolution discipline of predicted density under different pressure basically agrees with experimental densification behavior. The pressure–density curve is

Table 3
Key dimensions of the cuboid component before and after CIP.

	Initial dimensions (mm)	Experimental dimensions (mm)	Simulative dimensions (mm)	Experimental shrinkage rate (%)	Simulative shrinkage rate(%)	Relative error (%)
Length	51.20	42.58	42.80	16.80	16.41	0.5
Width	11.02	9.02	8.87	18.18	19.40	1.7
Height	9.82	7.52	7.91	23.47	19.24	5.2

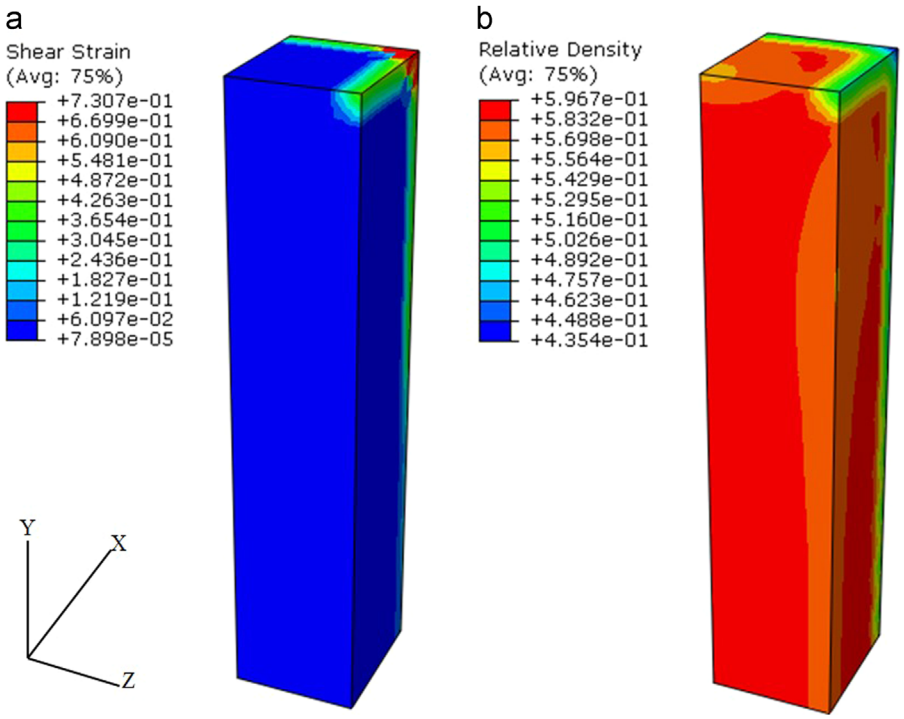

Fig. 5. Shear strain (a) and relative density distribution (b) contour of cuboid component after CIP (bag is not displayed).

characteristic of rapid linear densification in low pressure region and rapid hardening in high pressure region. According to the densification mechanism, the process can be divided into 3 stages. As shown in Fig. 10(a), large quantities of interconnected pores exist in the SLSed part. When CIP pressure rises from 0 to 150 MPa, the epoxy resin sintering necks with low strength are easily broken, thus densification is promoted by particle rearrangement rapidly. In stage II, when pressure increases from 150 MPa to 250 MPa, densification slows down. On one hand, as shown in Fig. 10(b), the deforming resistance force emerges from the increase of the contacting interfacial areas. On the other hand, the plastic flow of the epoxy resin and PVA promoted densification. Controlled by these two mechnisms, the densification rate decreases a little. In stage III, no obvious density changes can be discovered with pressure exceeding 250 MPa. This is the result of the sharp increase of the resistance force. However, it is difficult to include the effects of the plastic flow of small quantities of polymers in simulation. So the experimental density turns out a little higher than the simulative results when pressure exceeds 150 MPa.

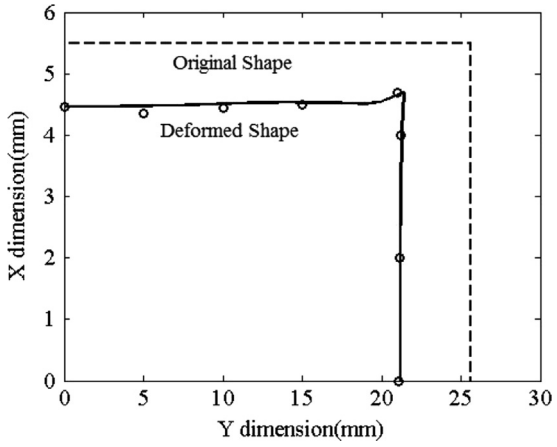

Fig. 6. Comparison of predicted and experimental shape of the cuboid components in *X*–*Y* plane. The experimental results are shown by solid lines, and simulative results by the hollow points.

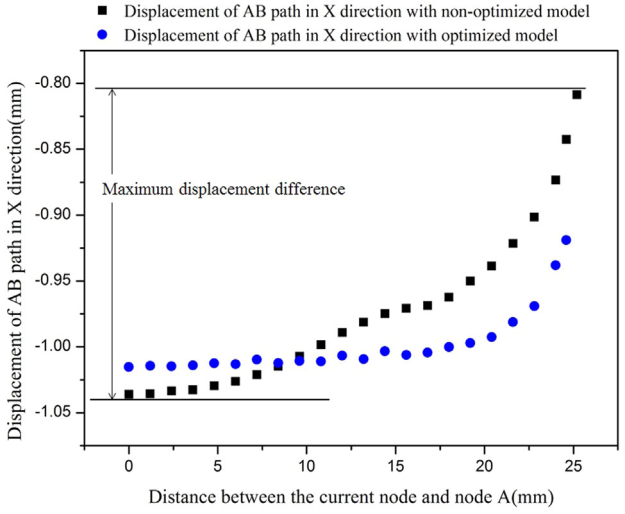

Fig. 7. Displacement of *AB* path in *X* direction of the cuboid model with and without optimized model.

4.2. CIP simulation of cuboid components with optimized models

Proper structure optimization of the components was investigated to decrease distortion and improve shape accuracy during CIP. Fillets with a radius of 0.5 mm were added to the cuboid component with other geometric parameters unchanged. The optimized model and its deformation after CIP are displayed in Fig. 11, in which no obvious distortion can be found. This indicates that fillets make it not easy for rubber bags to distort, helping uniformize the stress distribution on the surfaces of the model. The round points in Figs. 7 and 8 depict the displacement of path AB and B'C of the optimized model. The maximum displacement difference of AB path along *X*

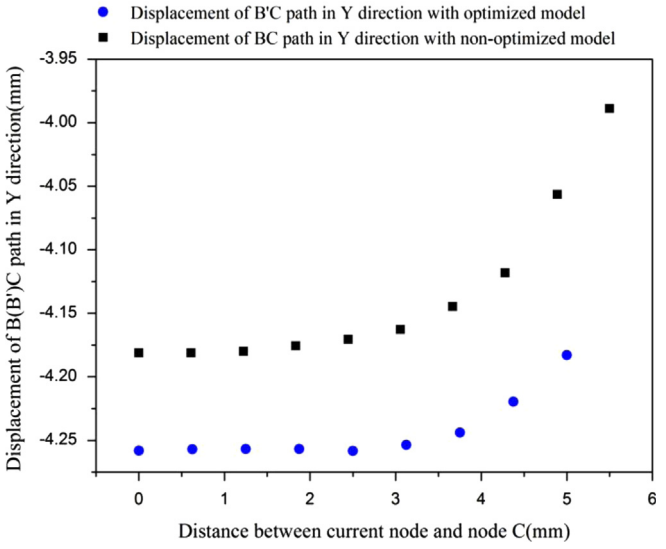

Fig. 8. Displacement of B(B′)C path in *Y* direction of the cuboid model with bag and optimized bag.

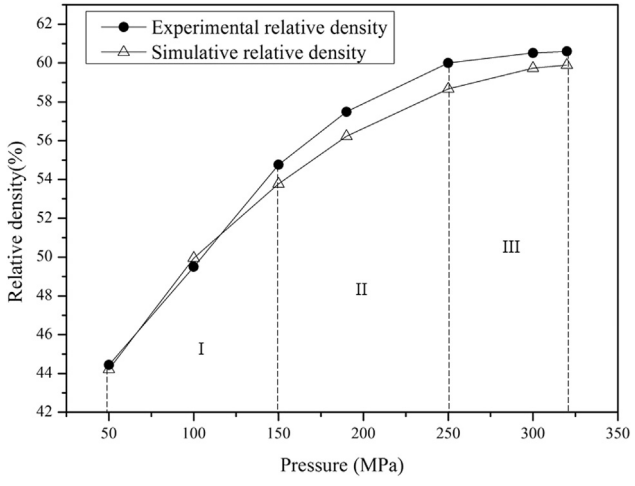

Fig. 9. The relative density of alumina SLS cuboid part under different CIP pressure.

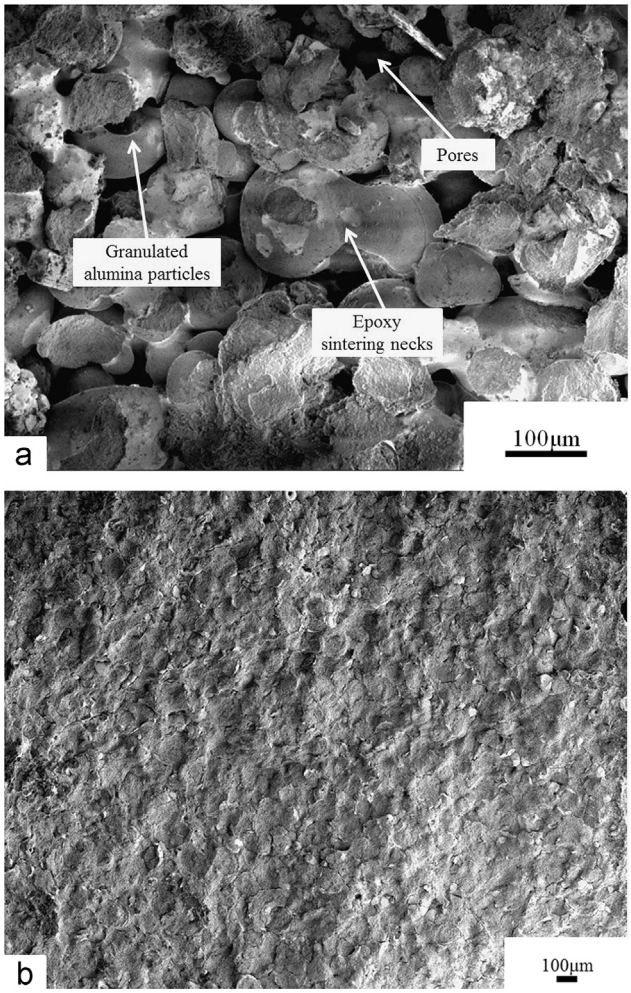

Fig. 10. The SEM photographs of fracture sections of cuboid components under (a) 0 MPa and (b) 200 MPa.

direction is 0.0682 mm, and the maximum difference of B'C path in *Y* direction is 0.0472 mm after CIP, both of which are much smaller than that of the model without optimization. Obviously the optimization results in less distortion as well as higher shape accuracy. As shown in Fig. 12(a), the peak shear strain along the corners is much less than that in Fig. 5(a). The optimization weakens the corner effects sharply. Seen from Figs. 5(b) and 12(b), no obvious difference is found between the maximum density of the models with and without optimization. Therefore, adding fillets is not supposed to help improve part density remarkably. However, it tends to homogenize the density distribution of the whole part, which facilitates the homogenization of mechanical properties of the CIPed parts.

4.3. Effects of fillet radius on densificatioin and deformation during CIP

The positive effects of fillets on reducing distortion and homogenization have been discussed in Section 4.2. The effects of fillet radius on densification and distortion of the model during CIP were studied. Fillet radius of 0.5 mm, 1 mm and 2 mm were selected as comparison groups by simulation.

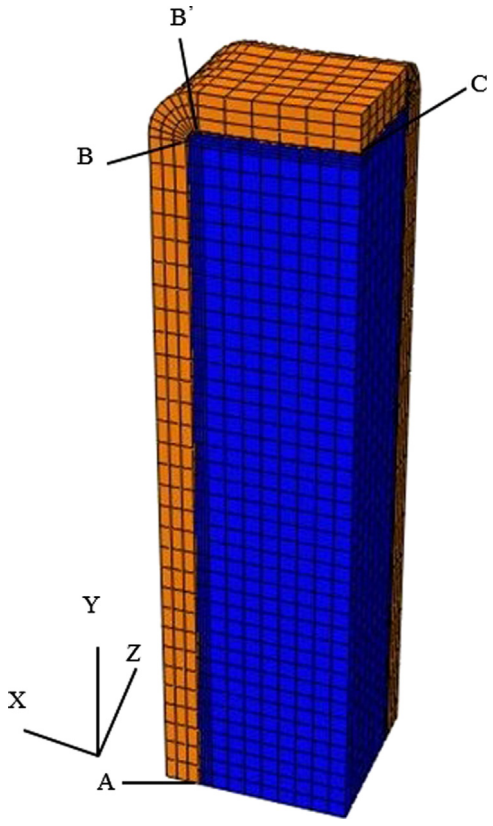

Fig. 11. The optimized model and its deformation after CIP.

Seen from Fig. 13, the maximum displacement difference of path AB with fillet radius of 0.5 mm is much larger than that with larger fillet radius in *X* direction. While the displacement difference with radius of 1 mm is much closer to that of 2 mm. The results indicate larger fillet brings about less distortion. While the advantageous influence turns to be obscure when the fillet becomes too large. Moreover, too large radius in turn leads to the performance and design disqualification of the working plane of the part. As shown in Fig. 14, it is notable that the dimensional shrinkage along Y direction increases sharply when the fillet radius increases from 0.5 mm to 1 mm. Hence larger fillet structure is supposed to provide favorable conditions for compaction. While due to the too small ratio of fillet radius to length, the positive influence cannot be easily detected in Fig. 13. Therefore, the optimal fillet radius can be concluded from the simulative results.

4.4. Final sintering results of the alumina components

Through optimization, the alumina cuboid parts reached their highest density of 62.5%, when pressed under 320 MPa. The alumina ceramic parts got their highest density of 94.5% through optimized sintering process, which is higher than the alumina part density prepared by reference [5]. Fig. 15 is the SEM micrograph of the part cross-section. The micrograph reveals the residual elongated pores between grains which were left after CIP and not completely eliminated by solid state sintering process, proving intergranular fracture as the main fracture form. It is due to the residual pores left between the

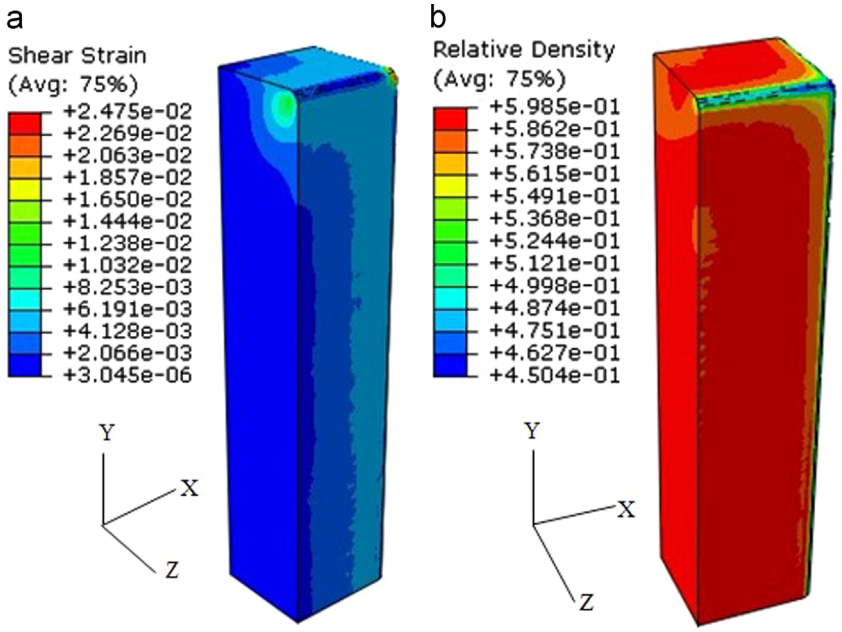

Fig. 12. Shear strain (a) and relative density distribution (b) contour of the optimized cuboid component after CIP (bag is not displayed).

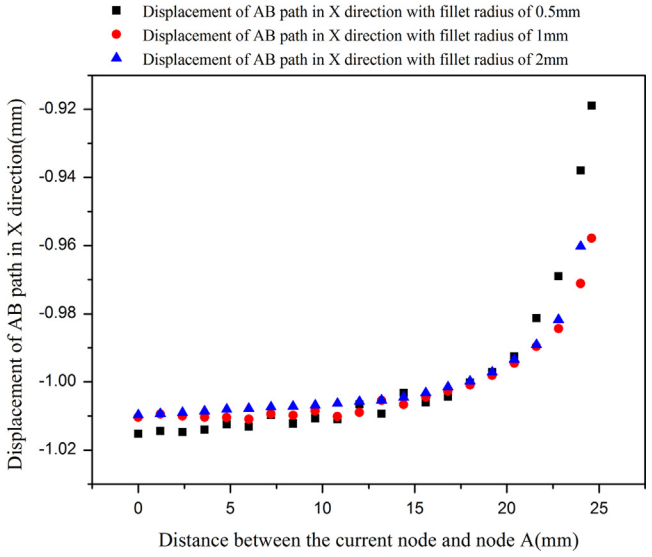

Fig. 13. Displacement of AB path in *X* direction of the cuboid model with different fillet radius.

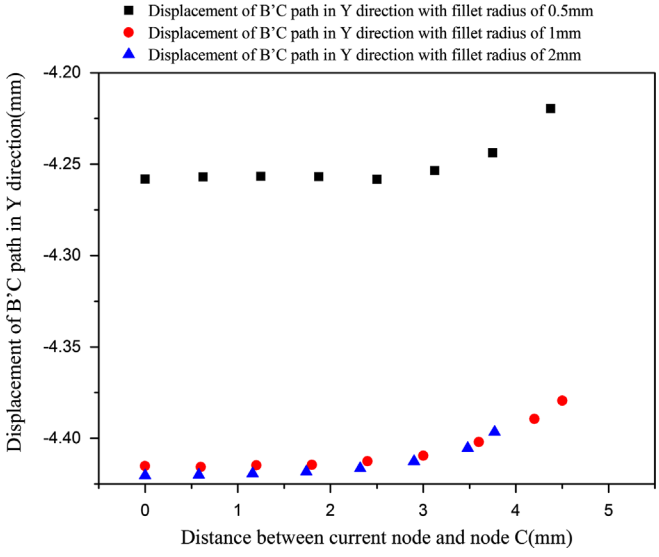

Fig. 14. Displacement of B'C path in *Y* direction of the cuboid model with different fillet radius.

alumina grains, which gives rise to the lower grain boundary strength.

5. Conclusions

The high-density alumina parts have been successfully produced by SLS/CIP compound process. With the optimized SLS, CIP and solid sintering processes, the alumina parts obtained its highest density of 94.5%. It proves effective and feasible that highly dense complex alumina parts can be produced by this process.

The CIP simulative results agree well with the experimental results. Their relative error is less than 1.7% in the forming plane, which highlights the significance of including rubber bags in simulation. Densification behavior was studied by both simulative and experimental methods, which reached a general accord. Proper structure optimization, namely adding fillets was made to reduce distortion and uniformize density distribution effectively.

Properly increasing the fillet radius can weaken part distortion and increase shape accuracy. Thus the optimal fillet radius can be determined by simulation comparison.

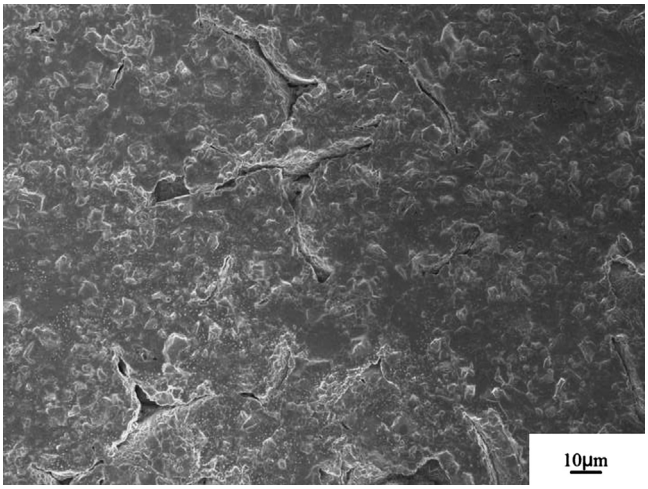

Fig. 15. SEM micrograph of alumina high temperature sintered parts.

Acknowledgments

This work was supported by National Science and Technology Support Program (2012BAF08B03) and Hubei Provincial Natural Science Foundation (2011CDB280).

References

[1] H.H. Tang, M.L. Chiu, H.C. Yen, Slurry-based selective laser sintering of polymer-coated ceramic powders to fabricate high strength alumina parts, Journal of the European Ceramic Society 31 (2011) 1383–1388.
[2] J.H. Du, J.K. Yan, N. Song, G.Y. Gan, Study on casting process of piezoelectric ceramics with complicated structure, Materials Science and Technology 14 (2006) 478–481.
[3] K. Shahzad, J. Deckers, S. Boury, B. Neirinck, J.P. Kruth, J. Vleugels, Preparation and indirect selective laser sintering of alumina/PA microspheres, Ceramics International 38 (2012) 1241–1247.
[4] R.J. Henderson, H.W. Chandler, A.R. Akisanya, B. Moriarty, Bag design in isostatic pressing, Materials and Design 21 (2000) 259–262.
[5] J. Deckers, K. Shahzad, S.J. Vleugel, J.P. Kruth, Isostatic pressing assisted indirect selective laser sintering of alumina components, Rapid Prototyping Journal 18 (2012) 409–419.
[6] Y.Y. Du, Y.S. Shi, Q.S. Wei, Finite element simulation of cold isostatic pressing of the selective laser-sintered components, Materials and Manufacturing Processes 25 (2010) 1389–1396.
[7] R.J. Henderson, H.W. Chandler, A.R. Akisanya, H. Barber, B. Moriarty, Finite element modelling of cold isostatic pressing, Journal of the European Ceramic Society 20 (2000) 1121–1128.
[8] M. Reiterer, T. Kraft, U. Janosovits, H. Riedel, Finite element simulation of cold isostatic pressing and sintering of SiC components, Ceramics International 30 (2004) 177–183.
[9] S.C. Lee, K.T. Kim, A study on the cap model for metal and ceramic powder under cold compaction, Materials Science and Engineering A-Structural Materials Properties Microstructure and Processing 445 (2007) 163–169.
[10] B. Hibbitt, ABAQUS Theory Manual, Elsevier Science Ltd, Netherland, 1996.
[11] R.B. Canto, V. Tita, J. De Carvalho, B. de M. Purguerio, Finite element simulation of ceramic powder isostatic pressing process using material parameters of a uniaxial compaction, Materials Science Forum 416–418 (2003) 561–566.
[12] Q.S. Wei, Y.Y. Du, B.B. Qu, Y.S. Shi, Densification of porous stainless-steel SLS components during cold isostatic pressing, Journal of Engineering Materials and Technology 132 (2010) 011015.
[13] W.X. Yuan, J. Mei, V. Samarov, D. Seliverstov, X. Wu, Computer modeling and tooling design for near net shaped components using hot isostatic pressing, Journal of Materials Processing Technology 182 (2007) 39–49.